

UV–Vis–NIR broadband response of GaAs-based photocathode with multilayer graded-band cascade structure

Ziheng Wang^a, Yijun Zhang^{a,*}, Yunsheng Qian^a, Shiman Li^a, Kaimin Zhang^a, Feng Shi^b, Hongchang Cheng^b, Gangcheng Jiao^b, Yugang Zeng^c

^a School of Electronic and Optical Engineering, Nanjing University of Science and Technology, Nanjing, 210094, China

^b Science and Technology on Low-Light-Level Night Vision Laboratory, Xi'an, 710065, China

^c Changchun Institute of Optics, Fine Mechanics and Physics, Chinese Academy of Sciences, Changchun, 130033, China

ARTICLE INFO

Keywords:

GaAs-based photocathode
Transmission-mode
Broadband response
Graded-band
Quantum efficiency
Lattice matching

ABSTRACT

To improve the lattice matching, quantum efficiency and response range of the transmission-mode GaAs-based photocathode, a novel photocathode with multilayer graded-band cascade emission layer is proposed. The one-dimensional steady-state continuity equations and finite-difference time-domain methods are utilized to obtain the quantum efficiency and optical absorption characteristics of the proposed photocathode, respectively. The results show that, the built-in electric fields generated by the varying-composition and varying-doping structure can assist the photoelectrons generated in the sublayer itself and the front sublayers to transport towards the emitting surface and escape to the vacuum. Compared with the conventional AlGaAs/InGaAs structure, the proposed structure possesses better lattice matching and enhanced quantum efficiency in the UV and NIR wavelength range. A three-fold increase of quantum efficiency can be realized at 400 nm and the theoretical quantum efficiency at 1064 nm can reach 2%. Besides, the integral absorptivity is increased by 6.8% in the visible wavelength range, and 12.9% in the NIR wavelength range. It is found that the increase of the thickness of AlGaAs sublayer and GaAs sublayer mainly reduces the quantum efficiency in the UV–Vis wavelength range. When the InGaAs sublayer is thin enough, the increase of thickness would enhance the quantum efficiency in the NIR wavelength range and deteriorate that in the UV–Vis wavelength range. This work can contribute to the performance improvement of UV–Vis–NIR broadband GaAs-based photocathode.

1. Introduction

Nowadays, extensive researches have been implemented on ultraviolet–visible–near infrared (UV–Vis–NIR) photodetectors, which offer widespread applications in optical communication, optical interconnects and high-resolution image sensing techniques [1–6]. Compared with solid-state photodetectors, vacuum photodetectors adopting various photocathodes have the advantages of high-speed response, low thermal noise, single photon detection and large detecting area [7–12]. In the application of conventional NIR photocathode, the imaging device relies on the transmission-mode photocathode, which works in the backside-illuminated situation. Such a cathode structure is commonly designed as the AlGaAs/InGaAs heterojunction structure [13–16]. However, the lattice

* Corresponding author.

E-mail address: zhangyijun423@126.com (Y. Zhang).

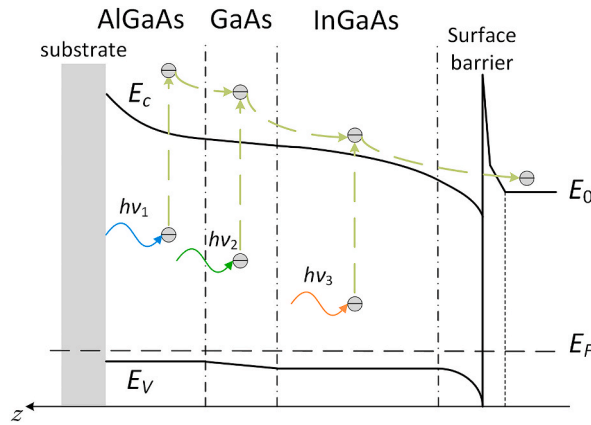


Fig. 1. Energy band structure diagram of the multilayer cascade emission layer. E_C is the minimum of conduction-band, E_V is the maximum of valence-band, E_F is the Fermi level, E_0 is the vacuum level, and hv_1 , hv_2 and hv_3 represent the incident photon energy in AlGaAs, GaAs and InGaAs, respectively.

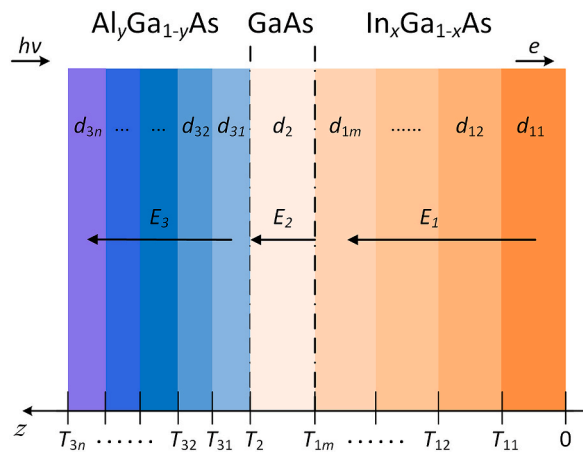


Fig. 2. Structure of the sublayers in the emission layer. d_{11-1m} denotes the thickness of each slice-layer of InGaAs material, d_2 is the thickness of GaAs sublayer, d_{31-3n} denotes the thickness of each slice-layer of AlGaAs material, T_{11-3m} represents the relative position between each slice-layer and emitting surface, and E_1 , E_2 , E_3 represent the built-in electric field in InGaAs sublayer, GaAs sublayer and AlGaAs sublayer, respectively.

mismatching problem between InGaAs and different material deteriorates the crystal quality of epitaxial InGaAs emission-layer, which will further limit the emission performance of photocathode [13,17,18].

As a significant performance parameter, the quantum efficiency of photocathode is related to the crystal quality and epitaxial structure [13,19]. With the development of semiconductor growth technology, the varying-doping and varying-composition structure can be realized on the preparation of photocathode. According to previous research, the built-in electric field generated by graded band gap arising from the varying-doping and varying-composition structure can significantly improve quantum efficiency of reflection-mode and transmission-mode AlGaAs/GaAs photocathodes [20–25]. Nevertheless, the effects of varying-doping and varying-composition structure on absorption of incident light in the emission-layer still needs to be studied. In addition, how to achieve the UV–Vis–NIR broadband response through reasonable structural design still requires further theoretical modeling and simulation.

A transmission-mode photocathode with a multilayer graded-band cascade structure is proposed to solve the lattice mismatching problem and improve the quantum efficiency, which combines the virtues of broadband UV–Vis–NIR response range, built-in electric fields and lattice matching. The corresponding theoretical quantum efficiency model of the transmission-mode photocathode with this multilayer complex structure is deduced by solving one-dimensional continuity equation. With the aid of the quantum efficiency model, the effect of built-in electron field on quantum efficiency is presented clearly. Meanwhile, the light absorption intensity distribution simulated by the finite-difference time-domain (FDTD) method is provided for comprehensive understanding. Besides, in order to clarify the relationship between the quantum efficiency and the emission-layer structural parameters, the quantum efficiency and absorptivity curves with different thicknesses of each sublayer in the multilayer cascade structure are also analyzed.

2. Structure and calculation

The energy band structure diagram of the transmission-mode photocathode with a multilayer cascade emission layer is shown in Fig. 1, wherein the emission layer consists of a varying-composition $\text{Al}_y\text{Ga}_{1-y}\text{As}$, a varying-doping GaAs and a varying-composition $\text{In}_x\text{Ga}_{1-x}\text{As}$. As shown in Fig. 1, the substrate is combined with the AlGaAs sublayer to serve as the self-supporting layer. According to the required optical transmission wavelength, the optical material such as quartz glass, borosilicate glass and sapphire is usually utilized as the substrate. The Al composition of $\text{Al}_y\text{Ga}_{1-y}\text{As}$ sublayer gradually decreases along the direction of electrons transport, which results in the narrowing of bandgap [26]. The wider bandgap of AlGaAs material is useful to prevent photoelectrons excited near the interface from being recombined in reverse. The GaAs sublayer with the constant bandgap has a varying-doping structure and the doping concentration decreases exponentially along the direction of electron movement. The sandwiched GaAs sublayer between $\text{Al}_y\text{Ga}_{1-y}\text{As}$ and $\text{In}_x\text{Ga}_{1-x}\text{As}$ can improve the lattice matching level and reduce the recombined electron loss at interface. The In composition of $\text{In}_x\text{Ga}_{1-x}\text{As}$ sublayer gradually increases along the direction of electron transport, which results in a gradual narrowing of the $\text{In}_x\text{Ga}_{1-x}\text{As}$ bandgap. The key strength of InGaAs material lies in its absorbing ability of NIR light. Since the semiconductor material in the equilibrium state has a uniform Fermi level inside, a band bending region, as shown in Fig. 1, is formed due to the Fermi level leveling effect. Because of the different absorption characteristics of materials, the short-wavelength incident light is mainly absorbed in AlGaAs sublayer, while the long-wavelength incident light is mainly absorbed in InGaAs sublayer. According to Spicer's three-step model [27], the photoelectrons are excited to conduction band, then transport towards the band bending region, and finally tunnel through the surface barrier. Due to the band-bending effect, the built-in electric fields are generated in each sublayer, wherein the direction of electric field is opposite to that of electron movement. The existence of built-in electric fields has the function of pulling electrons towards emitting surface and reducing reverse recombination loss [12,28–30].

Fig. 2 illustrates the internal structure of sublayers in the emission layer. The light is incident from the side of AlGaAs sublayer, and the excited electrons escape from the outermost surface of InGaAs sublayer. The $\text{Al}_y\text{Ga}_{1-y}\text{As}$ sublayer can be divided into a series of slice-layers with different Al composition along the z -axis. The Al composition of each slice-layers gradually increases along the direction of z -axis. The doping concentration of GaAs sublayer varies in the exponential form and increases along the direction of z -axis. The $\text{In}_x\text{Ga}_{1-x}\text{As}$ sublayer is also divided into several slice-layers with different In composition. The In composition of each slice-layers gradually decreases along the direction of z -axis. The corresponding built-in electric fields E_1 , E_2 and E_3 are generated inside each sublayer. Because of the graded-composition structure, the refractive index of slice-layers in the emission layer gradually increases along the light incident direction, which reduces light reflection loss in the process of propagation.

As can be seen from Fig. 2, the built-in electric fields E_1 , E_2 and E_3 are built in the corresponding $\text{In}_x\text{Ga}_{1-x}\text{As}$ sublayer, GaAs sublayer and $\text{Al}_y\text{Ga}_{1-y}\text{As}$ sublayer, respectively. Among them, E_1 and E_3 are generated by the varying-composition, and can be calculated by the following formulae:

$$E_1 = \frac{E_{g1m} - E_{g11}}{\sum_{ij=11}^{1m} d_{ij}} \quad (1)$$

$$E_3 = \frac{E_{g3n} - E_{g31}}{\sum_{ij=31}^{3n} d_{ij}} \quad (2)$$

where E_{g1m} and E_{g11} are the bandgap of the $1m$ -th and 11 -th slice-layer in the $\text{In}_x\text{Ga}_{1-x}\text{As}$ sublayer, E_{g3n} and E_{g31} are the bandgap of the $3n$ -th and 31 -th slice-layer in the $\text{Al}_y\text{Ga}_{1-y}\text{As}$ sublayer, d_{ij} is the thickness of the corresponding slice-layer. According to the relationship between Fermi level and doping concentration, the built-in electric field E_2 arising from the exponential-doping structure in the GaAs sublayer can be expressed by

$$N(T_2) = N(T_{1m})\exp(A \cdot d_2) \quad (3)$$

$$E_2 = \frac{k_0 T A}{q} \quad (4)$$

where $N(T_2)$ and $N(T_{1m})$ are the doping concentration on both sides of the GaAs sublayer, k_0 is the Boltzmann constant, T is the absolute temperature, q is the electron charge. According to Spicer's three-step model of photoemission, the quantum efficiency of this transmission-mode photocathode can be deduced from one-dimensional continuity equation [29], which is given by

$$D_{ij} \frac{d^2 n_{ij}(z)}{dz^2} + \mu_{ij} |E_i| \frac{dn_{ij}(z)}{dz} - \frac{n_{ij}(z)}{\tau_{ij}} + g_{ij}(z) = 0, \quad \begin{cases} i = 1, j = 1, 2, \dots, m \\ i = 2 \\ i = 3, j = 1, 2, \dots, n \end{cases} \quad (5)$$

where D_{ij} is the electron diffusion coefficient wherein the subscript ij represents the order number of slice-layer as shown in Fig. 2 μ_{ij} is electron mobility, E_i is the built-in electric field intensity, $n_{ij}(z)$ is the electron concentration, τ_{ij} is the lifetime of electron of sublayer, and $g_{ij}(z)$ is the generation function of photoelectrons in each sublayer. For the transmission-mode photocathode, the generation function can be obtained as follows

$$g_{ij}(z) = \begin{cases} (1 - R_{hv})I_0\alpha_{ij} \exp(-\alpha_{ij}(T_{ij} - z)) , i = 3, j = n \\ (1 - R_{hv})I_0\alpha_{ij} \left[\prod_{j'=j+1}^n \exp(-\alpha_{ij'}d_{ij'}) \right] \exp(-\alpha_{ij}(T_{ij} - z)) , i = 3, j \in [1, n - 1] \\ (1 - R_{hv})I_0\alpha_i \left[\prod_{j'=1}^n \exp(-\alpha_{3j'}d_{3j'}) \right] \exp(-\alpha_i(T_i - z)) , i = 2 \\ (1 - R_{hv})I_0\alpha_{ij} \left[\prod_{j'=1}^n \exp(-\alpha_{3j'}d_{3j'}) \right] \exp(-\alpha_2d_2) \exp(-\alpha_{ij}(T_{ij} - z)) , i = 1, j = m \\ (1 - R_{hv})I_0\alpha_{ij} \left[\prod_{j'=1}^n \exp(-\alpha_{3j'}d_{3j'}) \right] \exp(-\alpha_2d_2) \left[\prod_{j'=j+1}^m \exp(-\alpha_{ij'}d_{ij'}) \right] \exp(-\alpha_{ij}(T_{ij} - z)) , \\ i = 1, j \in [1, m - 1] \end{cases} \quad (6)$$

where R_{hv} is the reflectivity of photocathode, I_0 is the intensity of incident light, and α is the absorption coefficient of each slice-layer. To solve the continuity equation Eq. (5), the boundary conditions of each interface between slice-layers are given as follows:

$$\left[D_{ij} \frac{dn_{ij}(z)}{dz} + \mu_{ij}|E_i|n_{ij}(z) \right] \Big|_{z=T_{ij}} = [-S_{vij+1}n_{ij}(z) + S_{vij+1}n_{ij+1}(z)] \Big|_{z=T_{ij}} \quad (7)$$

$$\left[D_{ij} \frac{dn_{ij}(z)}{dz} + \mu_{ij}|E_i|n_{ij}(z) \right] \Big|_{z=T_{ij-1}} = S_{vij+1}n_{ij+1}(z) \Big|_{z=T_{ij-1}} \quad (8)$$

when $ij = 3n$, Eq. (7) is written as

$$\left[D_{3n} \frac{dn_{3n}(z)}{dz} + \mu_{3n}|E_3|n_{3n}(z) \right] \Big|_{z=T_{3n}} = -S_{v3n}n_{3n}(z) \Big|_{z=T_{3n}} \quad (9)$$

where S_{vij} represents the interface recombination velocity of corresponding slice-layer. When $ij = 11$, the electron concentration $n(0) = 0$. As for $\text{In}_x\text{Ga}_{1-x}\text{As}$ sublayer, the energy gap, electron diffusion coefficient and electron mobility are as functions of In composition, which are respectively given by [31].

$$E_g(x) = 0.36 + 0.63(1 - x) + 0.43(1 - x)^2 \text{ (eV)} \quad (10)$$

$$D(x) = [10 - 20.2(1 - x) + 12.3(1 - x)^2] \times 100 \text{ (cm}^2\text{s}^{-1}\text{)} \quad (11)$$

$$\mu(x) = 40 - 80.7(1 - x) + 49.2(1 - x)^2 \text{ (cm}^2\text{V}^{-1}\text{s}^{-1}\text{)} \quad (12)$$

Besides, the energy gap, electron diffusion coefficient, electron mobility and electrons lifetime of $\text{Al}_y\text{Ga}_{1-y}\text{As}$ also depend on the Al composition, and are given by [32,33].

$$E_g(y) = \begin{cases} 1.424 + 1.247y \text{ (eV)}, 0 \leq y \leq 0.45 \\ 1.9 + 0.125y + 0.143y^2 \text{ (eV)}, 0.45 < y < 1 \end{cases} \quad (13)$$

$$D(y) = \begin{cases} 200 - 500y + 250y^2 \text{ (cm}^2\text{s}^{-1}\text{)}, 0 \leq y \leq 0.45 \\ -6.4 + 29y - 18y^2 \text{ (cm}^2\text{s}^{-1}\text{)}, 0.45 < y < 1 \end{cases} \quad (14)$$

$$\mu(y) = \begin{cases} 8000 - 22000y + 10000y^2 \text{ (cm}^2\text{V}^{-1}\text{s}^{-1}\text{)}, 0 \leq y \leq 0.45 \\ -255 + 1160y - 720y^2 \text{ (cm}^2\text{V}^{-1}\text{s}^{-1}\text{)}, 0.45 < y < 1 \end{cases} \quad (15)$$

$$\tau(y) = 29.142 + \frac{4.444 - 29.142}{1 + e^{\frac{y-0.3443}{0.00468}}} \text{ (s)}, 0 \leq y < 1 \quad (16)$$

Through the above boundary conditions, the concentration of electrons of each slice-layer can be obtained by solving Eq. (5). After the concentration of electrons at the emitting surface $n_{11}(0)$ is obtained, the final quantum efficiency Y is calculated as follows

$$Y(h\nu) = PD_{11} \frac{dn_{11}(z)}{dz} \Big|_{z=0} / I_0 \quad (17)$$

where P is the surface electron escape probability. As for the transmission-mode $\text{AlGaAs/GaAs/InGaAs}$ photocathode with the uniform-composition or uniform-doping structure, the built-in electric fields E_1, E_2 or E_3 is equal to 0. In this case, the quantum efficiency can also be obtained in the same way.

Table 1
Parameters used in the simulation.

Parameter	Value	Description
S_{v35}	10^6 cm/s	Electron recombination at AlGaAs outermost interface
S_{v34-31}	10^5 cm/s	Electron recombination at AlGaAs interior interface
S_{v2}	10^4 cm/s (Ref. [9])	Electron recombination at AlGaAs/GaAs interface
S_{v14}	10^4 cm/s	Electron recombination at GaAs/InGaAs interface
S_{v13-11}	10^5 cm/s	Electron recombination at InGaAs interior interface
P	0.17 (Ref. [36])	Surface electron escape probability
L_{14}	1.2 μm (Ref. [37])	Electron diffusion length of $\text{In}_{0.05}\text{Ga}_{0.95}\text{As}$
L_{13}	1.1 μm (Ref. [37])	Electron diffusion length of $\text{In}_{0.1}\text{Ga}_{0.9}\text{As}$
L_{12}	0.9 μm (Ref. [37])	Electron diffusion length of $\text{In}_{0.15}\text{Ga}_{0.85}\text{As}$
L_{11}	0.8 μm (Ref. [36])	Electron diffusion length of $\text{In}_{0.2}\text{Ga}_{0.8}\text{As}$

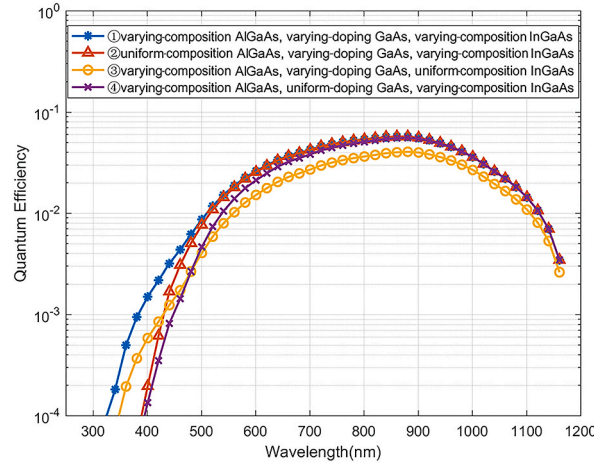


Fig. 3. Simulated quantum efficiency curves of AlGaAs/GaAs/InGaAs photocathodes with the four different emission layer structures.

3. Results and discussion

To simulate the quantum efficiency of the multilayer photocathode with the graded-band cascade structure, the structural parameters are assumed as follows: the $\text{Al}_y\text{Ga}_{1-y}\text{As}$ sublayer is divided into 5 slice-layers, and the proportions of Al composition of each slice-layer are 0.9, 0.675, 0.450, 0.225, and 0 respectively, along the direction of electron transport. Each slice-layer of AlGaAs sublayer has the same thickness of 0.02 μm and the same doping concentration of $1 \times 10^{19} \text{ cm}^{-3}$. As for the GaAs sublayer, the thickness is 0.15 μm and the doping concentration decreases exponentially from $1 \times 10^{19} \text{ cm}^{-3}$ to $1 \times 10^{18} \text{ cm}^{-3}$, along the direction of electron transport as well. Considering that the lattice mismatching problem will become more serious with the increase of In composition and $\text{In}_{0.2}\text{Ga}_{0.8}\text{As}$ has enough high absorption ability of 1064 nm light, the $\text{In}_x\text{Ga}_{1-x}\text{As}$ sublayer is divided into 4 slice-layers with the In composition of 0.05, 0.1, 0.15 and 0.2 from bulk to surface. The doping concentration of each slice-layer of $\text{In}_x\text{Ga}_{1-x}\text{As}$ sublayer is $1 \times 10^{18} \text{ cm}^{-3}$. In view of the absorption ability of 1064 nm light in $\text{In}_{0.2}\text{Ga}_{0.8}\text{As}$, the thickness of each slice-layer is assumed to be 0.05 μm , 0.05 μm , 0.05 μm and 0.7 μm from the inner to the emission surface. In addition, the refractive index and extinction coefficient of AlGaAs and GaAs are referred to Ref. [34], while the refractive index and extinction coefficient of InGaAs are referred to Ref. [35]. In order to highlight the difference in quantum efficiency curves of different emission layer structures, herein, the value of the reflectivity R_{ny} is set to be 0.31 when calculating quantum efficiency [29], while the other parameters utilized in the simulations are listed in Table 1. Furthermore, the optical absorption characteristics of the transmission-mode photocathode, such as absorptivity and absorption intensity distribution can be calculated by the FDTD method. In the simulation of optical property, the emission layer is illuminated by a plane wave beam as light source starting from vacuum space, the incident light is perpendicular to the AlGaAs surface, and the virtual light power monitors are placed above the light source and the bottom of InGaAs sublayer, respectively. In this case, the emission layer structure can be treated as one-dimensional model in FDTD calculation along the z-axis, and the emission layer can be regarded as a periodic material in the x-axis direction.

In order to investigate the effect of varying-composition and varying-doping structure on quantum efficiency, the other three emission layer structures are given for comparison. As shown in Fig. 3, the curve 1 represent the quantum efficiency curve of the emission structure we designed above, which composes a varying-composition AlGaAs sublayer, a varying-doping GaAs sublayer and a varying-composition InGaAs sublayer. In structure 2, the varying-composition AlGaAs sublayer is replaced by a uniform-composition $\text{Ga}_{0.5}\text{Al}_{0.5}\text{As}$ sublayer, of which the thickness is the same as that of $\text{Al}_y\text{Ga}_{1-y}\text{As}$ sublayer in structure 1, and the electron recombination velocity at $\text{Ga}_{0.5}\text{Al}_{0.5}\text{As}/\text{GaAs}$ interface increases to $1 \times 10^6 \text{ cm/s}$ in view of the deteriorated lattice mismatch. In structure 3, the

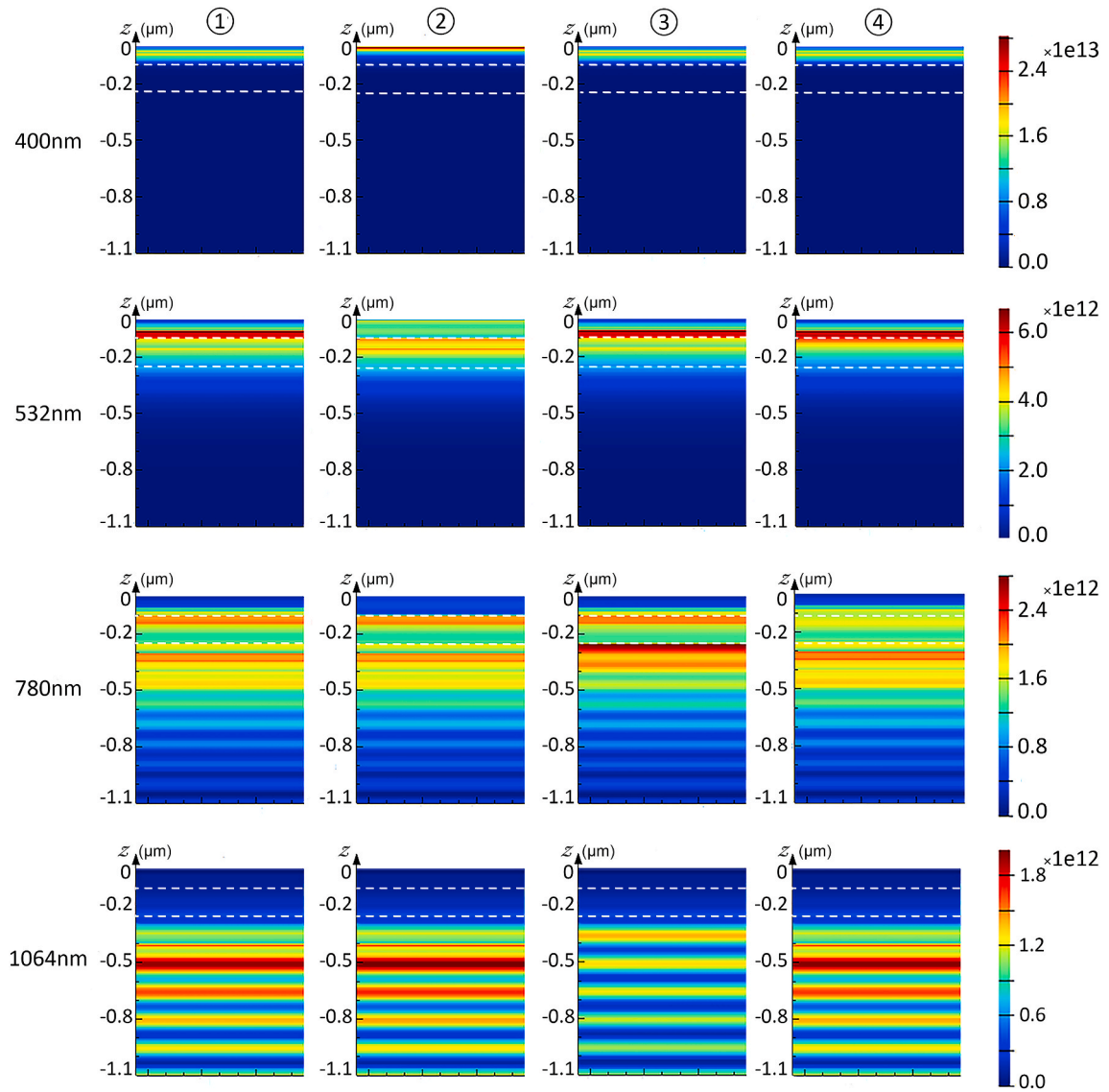


Fig. 4. Absorption intensity distribution at specific wavelengths of AlGaAs/GaAs/InGaAs photocathodes with the four different emission layer structures.

varying-composition $\text{In}_x\text{Ga}_{1-x}\text{As}$ sublayer is replaced by a uniform-composition $\text{In}_{0.1}\text{Ga}_{0.9}\text{As}$ sublayer, of which the thickness is the same as that of $\text{In}_x\text{Ga}_{1-x}\text{As}$ sublayer in structure 1, and the electron recombination velocity at GaAs/ $\text{In}_{0.1}\text{Ga}_{0.9}\text{As}$ interface increases to 1×10^6 cm/s because of the deteriorated lattice mismatching problem as well. In structure 4, the varying-doping GaAs sublayer is replaced by a uniform-doping GaAs sublayer with the same thickness, of which the doping concentration is 1×10^{19} cm^{-3} . The thickness of all remaining sublayers in the other three structures is the same as that in structure 1. As shown in Fig. 3, it is noted that curve 1 corresponding to the proposed structure 1 exhibits the widest spectral range and the highest quantum efficiency, which indicates the advantage of the multilayer graded-band cascade structure. Compared with curve 2, it is found that the structure 1 has higher quantum efficiency when the incident light wavelength is shorter than 500 nm. The incident light with the wavelength shorter than 500 nm is almost completely absorbed by the AlGaAs sublayer. In the varying-composition AlGaAs sublayer, the excited photoelectrons assisted by the built-in electric field in AlGaAs sublayer have longer diffusion distance and higher probability to reach the GaAs sublayer and further move towards the emitting surface. Because of the diffusion and migration effect, more photoelectrons excited by light wavelength shorter than 500 nm can reach the emitting surface and escape into vacuum for structure 1. Besides, it can be found that the structure 4 has lower quantum efficiency when the wavelength of incident light is shorter than 800 nm, which is ascribed from the uniform-doping GaAs sublayer. As a result of the absence of the built-in electric field in GaAs sublayer, less excited electrons in AlGaAs sublayer and GaAs sublayer can reach the InGaAs sublayer. As shown in Fig. 3, the quantum efficiency curve of structure 3 is lower than that of structure 1 in the entire spectral range. It is noted that all the excited photoelectrons must reach the

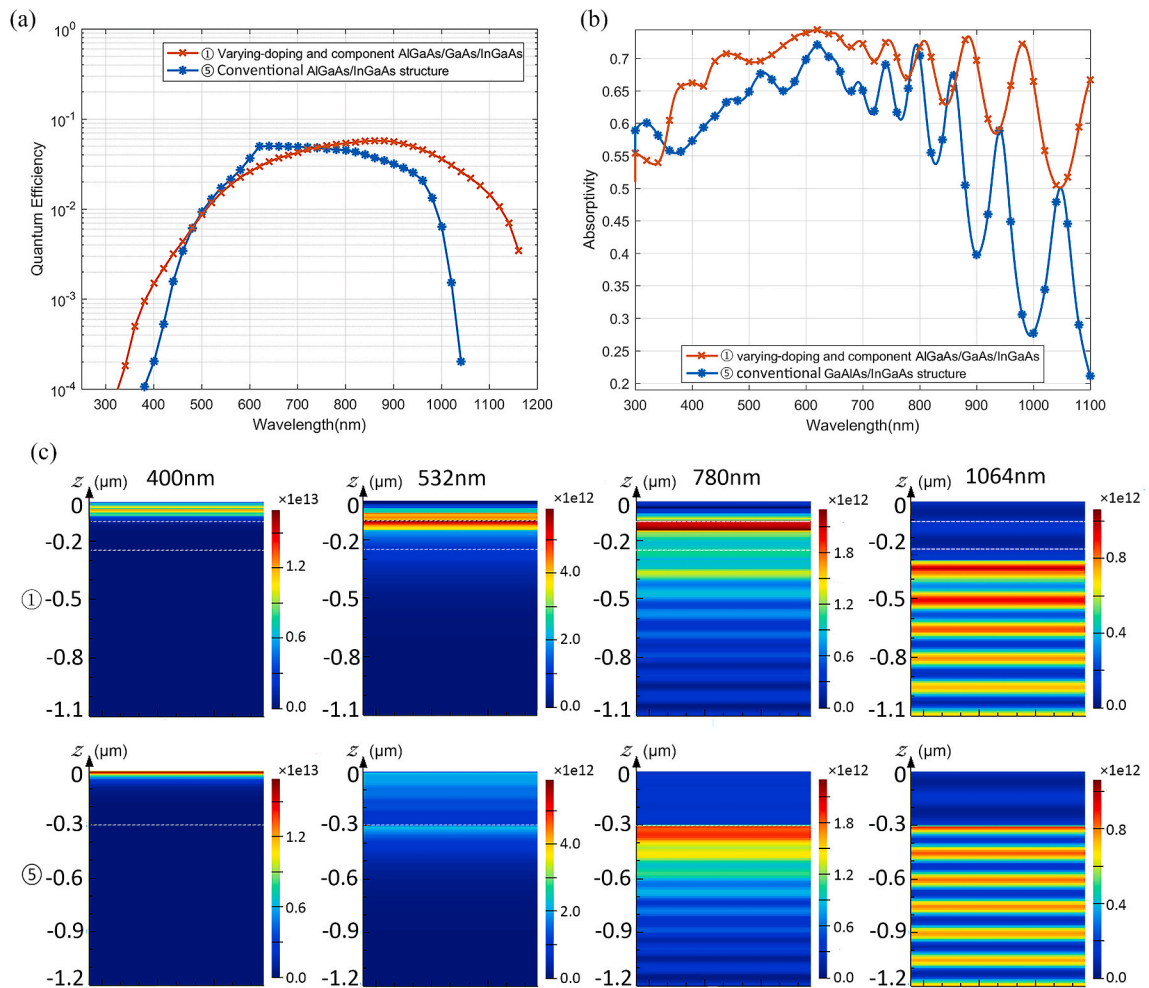


Fig. 5. (a) Quantum efficiency curves, (b) absorptivity curves and (c) absorption intensity distribution of the conventional AlGaAs/InGaAs photocathode and proposed AlGaAs/GaAs/InGaAs photocathode.

InGaAs emission surface to escape into vacuum, which means that the built-in electric field in InGaAs sublayer affects the electrons generated by incident light of all wavelengths. In this case, the varying-composition structure of InGaAs sublayer is especially important for improving UV-Vis-NIR broadband response because the absence of built-in electric field in InGaAs sublayer can decrease the whole quantum efficiency spectrum.

For the purpose of fully understanding the participation of different sublayers in the absorption process at different light wavelengths, the absorption intensity distribution diagrams of aforementioned four structures at different light wavelengths are shown in Fig. 4, wherein each column corresponds to the light absorption intensity distribution diagrams of the same structure at different light wavelength, and each row represents the light absorption intensity distribution diagrams of four different structures at the same light wavelength. The incident light wavelengths of 400 nm, 532 nm, 780 nm and 1064 nm are chosen as examples. It is found that the 400 nm incident light is absorbed in AlGaAs sublayer solely, the 532 nm incident light is absorbed by AlGaAs and GaAs sublayers, the 780 nm incident light is mainly absorbed by GaAs and InGaAs sublayers together, and the 1064 nm incident light is absorbed in InGaAs sublayer. As seen from columns 1 and 2 in Fig. 4, it is noted that the absorption intensity distribution diagrams of structure 1 and structure 2 are obviously different at 400 nm and 532 nm wavelength. Because the lower Al composition corresponds to a higher absorption rate for 400 nm and 532 nm wavelength, the varying-composition $\text{Al}_y\text{Ga}_{1-y}\text{As}$ sublayer has better absorption for the incident light at these two wavelengths, while the 400 nm light is completely absorbed at the surface of uniform-composition AlGaAs sublayer and the 532 nm light is mainly absorbed in the GaAs sublayer. Since the 400 nm and 532 nm incident light are completely absorbed before reaching InGaAs sublayer, the absorption capacity at the two wavelengths is the same for these four structures. As shown in Fig. 4, the absorption at 1064 nm wavelength of structure 3 is much worse than that of structure 1. Because of varying composition and lattice matching, the higher In composition $\text{In}_{0.2}\text{Ga}_{0.8}\text{As}$ slice-layer can be obtained in structure 1, which has much better absorption at 1064 nm wavelength than $\text{In}_{0.1}\text{Ga}_{0.9}\text{As}$. As for structure 3, the 780 nm incident light is almost completely absorbed in InGaAs sublayer near GaAs sublayer, which is different from structure 1 with varying-composition $\text{In}_x\text{Ga}_{1-x}\text{As}$ sublayer. In addition, the absorption

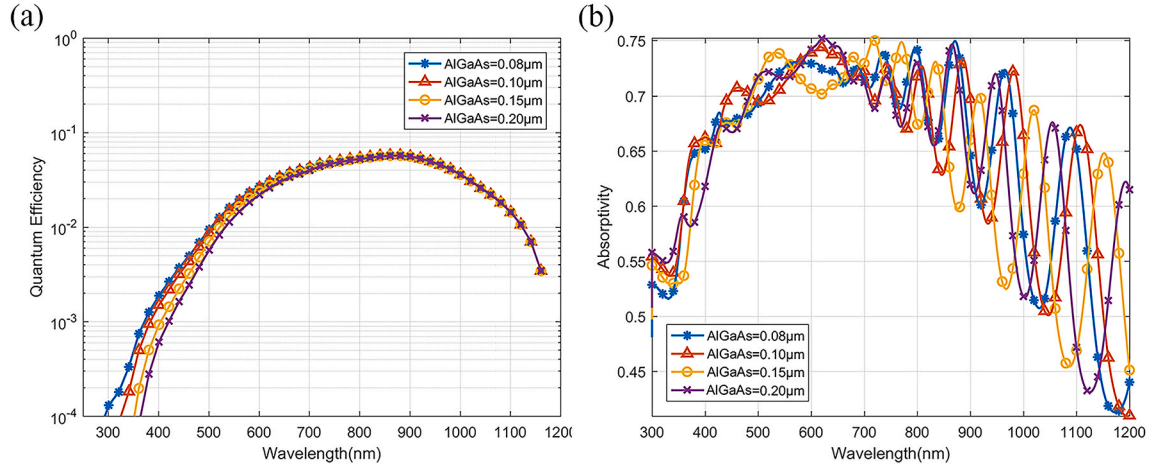


Fig. 6. (a) Quantum efficiency curves and (b) absorptivity curves of corresponding structure with different AlGaAs sublayer thicknesses.

intensity distribution of 780 nm light for structure 4 is also different from that for structure 1. Due to the lower absorption coefficient at 780 nm for GaAs with the higher doping concentration, the uniform-doping GaAs sublayer in structure 4 has worse absorption of 780 nm light. According Fig. 4, it can be found that, for the UV–Vis incident light that can be completely absorbed, the change of structure only adjusts the absorption depth. However, for the NIR incident light that cannot be absorbed completely, the structure with varying-composition InGaAs sublayer can greatly increase the absorption capacity.

To further verify the superiority of the proposed structure, the quantum efficiency of conventional uniform-composition and uniform-doping AlGaAs/InGaAs structure is also simulated, as shown in Fig. 5(a). The absorptivity curves and absorbing intensity distribution diagrams of the proposed and conventional structures are exhibited in Fig. 5(b) and (c) respectively. In Fig. 5(c), the row of diagrams represents the absorption intensity distribution of the same structure at different light wavelengths, while the column of diagrams represents the absorption intensity distribution of different structures at the same light wavelength. According to reference [13], the photocathode with conventional AlGaAs/InGaAs structure consists of a 0.3 μm thick Ga_{0.5}Al_{0.5}As window layer and a 0.9 μm thick In_{0.1}Ga_{0.9}As active layer. The electron recombination velocity at the Ga_{0.5}Al_{0.5}As/In_{0.1}Ga_{0.9}As interface is set as 1×10^7 cm/s, because of the serious lattice mismatching. As Fig. 5(a) shows, the quantum efficiency of proposed structure is higher than that of conventional structure in UV and NIR wavelength range, while the conventional structure has higher quantum efficiency in the wavelength range of 500–750 nm. On the one hand, with the assist of built-in electric field of multilayer graded-band cascade structure, the excited photoelectrons generated by the light wavelength less than 500 nm obtain longer migration distance to reach the emitting surface. On the other hand, because of the varying-composition structure, the absorption depth of light wavelength less than 500 nm in the proposed structure is deeper than that of conventional structure, as shown in Fig. 5(c), which shortens the transport distance to the emitting surface. Through the varying-composition growth, the In_xGa_{1-x}As sublayer with higher In composition can be obtained in the proposed structure, which has better absorptivity in the range from 800 nm to 1200 nm than the conventional In_{0.1}Ga_{0.9}As sublayer, as shown in Fig. 5(b) and (c). Due to the light absorption characteristics of In_{0.1}Ga_{0.9}As and Ga_{0.5}Al_{0.5}As, the incident light in the range from 500 nm to 750 nm cannot be absorbed completely in Ga_{0.5}Al_{0.5}As sublayer, as shown in Fig. 5(c). In this case, the light in this range can be absorbed in the InGaAs sublayer for the conventional structure, and excites the electrons closer to the emitting surface, which causes the higher quantum efficiency in the range of 500–750 nm. As shown in Fig. 5(b), the proposed varying-composition In_xGa_{1-x}As sublayer improves the shortcoming of insufficient absorption in the NIR wavelength range for the conventional structure. In order to better quantify the absorption capacity of the different structure, the integral absorptivity is introduced, which is given by Ref. [38]:

$$A_f = \frac{1}{\lambda_2 - \lambda_1} \int_{\lambda_1}^{\lambda_2} A_{hv} d\lambda \quad (18)$$

where A_f is the integral absorptivity, A_{hv} is the spectral absorptivity, and λ_1 and λ_2 are the start and cut-off wavelength respectively. According to Eq. (18), the calculated integral absorptivity of the proposed structure and the conventional structure is 85.1% and 79.7% in the visible wavelength range (i.e. 380–780 nm), respectively. In addition, in the NIR wavelength range (i.e. 780–1100 nm), the calculated integral absorptivity of the two structures is 55.9% and 49.5%, respectively. In contrast to the conventional structure, the integral absorptivity of the proposed structure is increased by 6.8% in the visible wavelength range, and 12.9% in the NIR wavelength range. As shown in Fig. 5(a) and (c), the proposed structure has better absorption of 1064 nm light, and thus the quantum efficiency of the proposed structure is higher than that of the conventional structure in the wavelength range over 800 nm combined with the function of built-in electric field.

In addition, the quantum efficiency curves of the proposed structure with different sublayers thicknesses are simulated for obtaining the optimal thickness of each sublayer. Fig. 6 exhibits the quantum efficiency curves and corresponding absorptivity curves

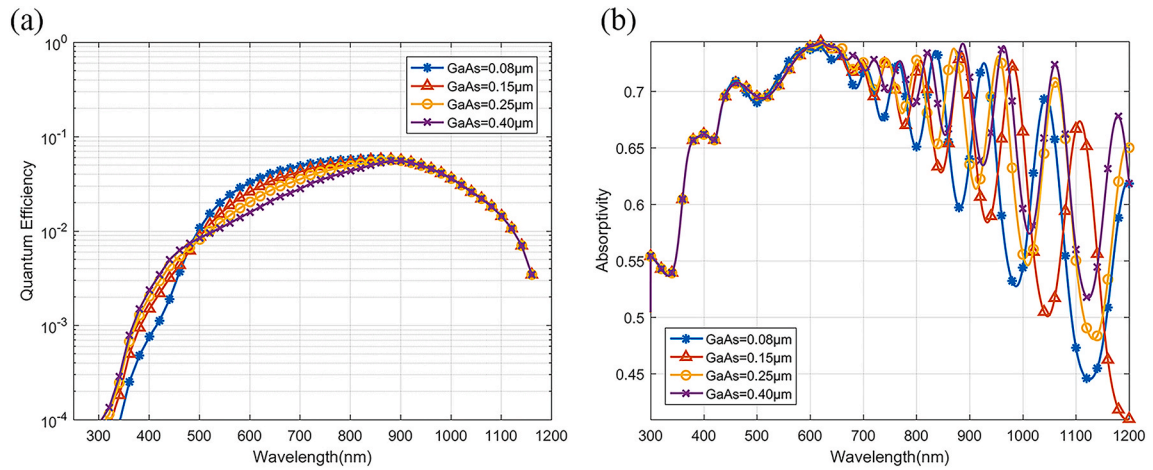


Fig. 7. (a) Quantum efficiency curves and (b) absorptivity curves of corresponding structure with different GaAs sublayer thicknesses.

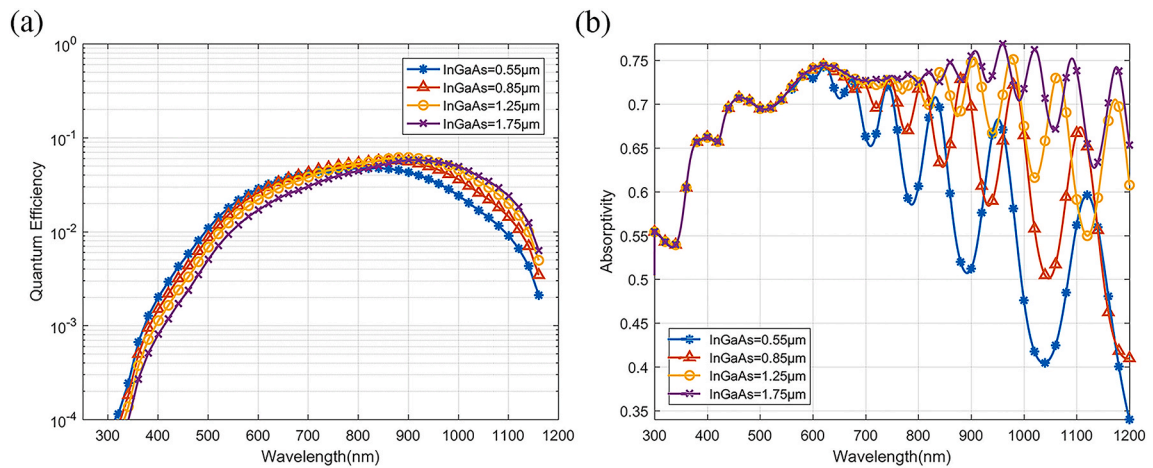


Fig. 8. (a) Quantum efficiency curves and (b) absorptivity curves of corresponding structure with different InGaAs sublayer thicknesses.

of the proposed structure with different AlGaAs sublayer thicknesses, while the thicknesses of GaAs and InGaAs sublayer remain unchanged. According to Fig. 6(a), it is noted that the quantum efficiency in the wavelength range less than 700 nm gradually decreases with the thickness of AlGaAs sublayer increasing. According to the absorption intensity distribution in Fig. 4, the varying-composition AlGaAs sublayer participates in the absorption of incident light with wavelength less than 700 nm. Because the incident light within the wavelength range is entirely absorbed in emission layer, the increase of AlGaAs sublayer thickness would lengthen the transport distance of excited electrons. On the other hand, according to Eq. (1), the increase of AlGaAs sublayer thickness decreases the built-in electric field intensity and weakens the effect of built-in electric field on excited electrons. Because the AlGaAs sublayer serves as a barrier and reflector for reverse electron transport and a supporting and thermal protective layer for thermal bonding to glass, the AlGaAs sublayer must have sufficient thickness. These quantum efficiency curves have no difference over 700 nm wavelength, because the long-wavelength incident light cannot be absorbed in AlGaAs sublayer. As shown in Fig. 6(b), the change of AlGaAs sublayer thickness has no obvious influence on the absorptivity shape except the wavelength position of peaks and valleys. With the increase in the thickness of AlGaAs sublayer, the positions of peaks and valleys shift towards the long wavelength. In combination with Fig. 6(a) and (b), it can be inferred that the increase of the thickness of AlGaAs sublayer can mainly influence the transport of electrons excited by the light with wavelength less than 700 nm, which degrades the quantum efficiency within this wavelength range.

Fig. 7 exhibits the changes of quantum efficiency and absorptivity curves with different GaAs sublayer thicknesses. As shown in Fig. 7(a), with the increase of GaAs sublayer thickness, the quantum efficiency spectrum at the wavelength less than 900 nm decreases obviously. Because the AlGaAs sublayer and GaAs sublayer have no ability to absorb light with wavelengths exceeding 900 nm, the incident light in this wavelength range is only absorbed in the InGaAs sublayer. For the incident light at the wavelength which can be fully absorbed in the emission layer, the increase of GaAs sublayer thickness lengthens the transport distance of the excited electrons, which causes the decrease of quantum efficiency. The absorptivity curves with different GaAs sublayer thicknesses are shown in Fig. 7

(b). According to the diagram, the thickness of GaAs sublayer has no obvious effect on the absorptivity curve at the wavelength less than 700 nm. Because the incident light in the wavelength range 700–900 nm cannot be absorbed completely when the GaAs sublayer is thin enough, as the thickness of GaAs sublayer increases, the absorptivity at the wavelength less than 900 nm gradually achieves the maximum, while the positions of peaks and valleys of absorptivity curve shift towards the long wavelength.

As the main component of the emission layer, the thickness of InGaAs sublayer is one of the most vital parameters for the quantum efficiency of the proposed photocathode. Fig. 8(a) exhibits the quantum efficiency curves with different thicknesses of InGaAs sublayer for comparison. As shown in Fig. 8(a), when the thickness of InGaAs sublayer gradually increases, the quantum efficiency in the UV–Vis wavelength range decreases, while the quantum efficiency increases in the NIR wavelength range. It can also be found that the intersections of different quantum efficiency curves shift towards the long wavelength with the thickness of InGaAs sublayer increases. When the InGaAs sublayer gets thicker, the light that cannot be absorbed completely originally is fully absorbed, and the transport distance of excited electrons is lengthened with the increase of the thickness. Hence, the intersection position of quantum efficiency gets shifted towards the long wavelength along with the increase of the thickness of InGaAs sublayer. Meanwhile, the increase of the thickness of InGaAs sublayer lengthens the transport distance of the electrons excited in AlGaAs sublayer and GaAs sublayer. Because of the absorbing ability of AlGaAs and GaAs, the incident light at the wavelength over 900 nm can only be absorbed in the InGaAs sublayer, and the incident light in this range cannot be absorbed completely when the InGaAs sublayer is not thick enough. In this case, the thicker InGaAs sublayer provides longer absorption distance and better absorptivity in the NIR wavelength range. When the thickness of InGaAs sublayer exceeds 2.2 μm , the quantum efficiency at 1064 nm becomes decreased with the further increase of the InGaAs thickness. The absorptivity curves of different InGaAs sublayer thickness are also shown in Fig. 8(b). It can be seen that the increase of the thickness of InGaAs sublayer can greatly enhance the absorptivity in the NIR wavelength range, while the absorptivity in the UV–Vis range remains unchanged since the light in this wavelength range is fully absorbed in AlGaAs and GaAs sublayers.

4. Conclusion

In summary, a novel transmission-mode GaAs-based photocathode with the multilayer graded-band cascade structure is proposed, which combines the virtues of UV–Vis–NIR broadband response range, lattice matching and quantum efficiency improvement. The quantum efficiency and optical absorption characteristics of proposed photocathode structure are investigated based on the one-dimensional continuity equation and FDTD method. According to the simulated results of photocathodes with different structures, the varying-composition and varying-doping structure can enhance the quantum efficiency in the UV and NIR wavelength range. It is found that the built-in electric field in each sublayer contributes to the photoelectrons generated in the sublayer itself and the front sublayers. Through the varying-composition structure, the proposed structure possesses better absorption ability in the NIR wavelength range and shortens the transport distance of electron excited in AlGaAs sublayer and GaAs sublayer. Moreover, the quantum efficiency and absorptivity curves of the proposed structure with different sublayer thickness are systematically compared. It is found that the increase of the thickness of AlGaAs sublayer and GaAs sublayer mainly decreases the quantum efficiency in the UV–Vis wavelength range, while that of the InGaAs sublayer has different effects on the quantum efficiency in UV–Vis and NIR wavelength range, respectively. This work can provide theoretical guidance for optimal design of the broadband response transmission-mode photocathode.

Declaration of competing interest

The authors declare that they have no known competing financial interests or personal relationships that could have appeared to influence the work reported in this paper.

Acknowledgments

The project was supported by the National Natural Science Foundation of China (Grant Nos. 61771245, 61301023) and the Science and Technology on Low-Light-Level Night Vision Laboratory Foundation of China (Grant No. J20200102).

References

- [1] Y. Zhang, Y.Q. Yu, L.F. Mi, H. Wang, Z.F. Zhu, Q.Y. Wu, Y.G. Zhang, Y. Jiang, *Small* 12 (2016) 1062–1071.
- [2] L. Ye, H. Li, Z.F. Chen, J.B. Xu, *ACS Photonics* 3 (2016) 692–699.
- [3] G. Chen, B. Liang, X. Liu, Z. Liu, G. Yu, X.M. Xie, T. Luo, D. Chen, M.Q. Zhu, G.Z. Shen, Z.Y. Fan, *ACS Nano* 8 (2014) 787–796.
- [4] H.L. Zhu, Z.F. Liang, Z.B. Huo, W.K. Ng, J. Mao, K.S. Wong, W.J. Yin, W.C.H. Choy, *Adv. Funct. Mater.* 28 (2018) 1706068.
- [5] B. Tiwari, M.J. Hossain, I. Bhattacharya, *Sol. Energy* 135 (2016) 618–624.
- [6] Z.C. Wang, B. Tian, M. Pantouvaki, W. Guo, P. Absil, J.V. Campenhout, C. Merckling, D.V. Thourhout, *Nat. Photonics* 9 (2015) 837–842.
- [7] H. Dömer, O. Bostanjoglo, *Rev. Sci. Instrum.* 74 (2003) 4369–4372.
- [8] J. Blacksberg, Y. Maruyama, E. Charbon, G.R. Rossman, *Opt. Lett.* 36 (2011) 3672–3674.
- [9] J.W. Schwede, T. Sarmiento, V.K. Narasimhan, S.J. Rosenthal, D.C. Riley, F. Schmitt, I. Bargatin, K. Sahasrabudhe, R.T. Howe, J.S. Harris, N.A. Melosh, Z. X. Shen, *Nat. Commun.* 4 (2013) 1576.
- [10] G.Y. Wang, B.K. Chang, M.J. Yang, K. Wang, H.C. Tran, J. Liu, R.G. Fu, Y.S. Qian, F. Shi, H.C. Cheng, *Sol. Energy* 174 (2018) 352–358.
- [11] G. Xiao, G.H. Zheng, M. Qiu, Q. Li, D.S. Li, M.J. Ni, *Appl. Energy* 208 (2017) 1318–1342.
- [12] S. Karkare, L. Boulet, L. Cultrera, B. Dunham, X.H. Liu, W. Schaff, I. Bazarov, *Phys. Rev. Lett.* 112 (2014), 097601.
- [13] H.C. Cheng, Q.D. Duanmu, S. Peng, Y. Lei, H. Liu, *Optoelectron. Adv. Mater. Rapid Commun.* 6 (2012) 788–792.

- [14] T. Nishitani, T. Nakanishi, M. Yamamoto, S. Okumi, F. Furuta, M. Miyamoto, M. Kuwahara, N. Yamamoto, K. Naniwa, O. Watanabe, Y. Takeda, H. Kobayakawa, Y. Takashima, H. Horinaka, T. Matsuyama, K. Togawa, T. Saka, M. Tawada, T. Omori, Y. Kurihara, M. Yoshioka, K. Kato, T. Baba, *J. Appl. Phys.* 97 (2005), 094907.
- [15] R. Nötzel, J. Temmyo, T. Tamamura, *Nature* 369 (1994) 131–133.
- [16] T. Matsuyama, M. Mukai, H. Horinaka, K. Wada, T. Nakanishi, S. Okumi, K. Togawa, T. Nishitani, T. Baba, *Jpn. J. Physiol.* 40 (2001) 6468–6472.
- [17] O. Yastrubchaka, T. Wosinski, T. Figielski, E. Lusakowska, B. Peczek, A.L. Toth, *Phys. E* 17 (2003) 561–563.
- [18] D.T. Neilson, L.C. Wilkinson, D.J. Goodwill, A.C. Walker, B. Vogeles, M. McElhinney, F. Pottier, C.R. Stanley, *Appl. Phys. Lett.* 70 (1997) 2031–2033.
- [19] M.C. Jin, X.L. Chen, G.H. Hao, B.K. Chang, H.C. Cheng, *Appl. Opt.* 54 (2015) 8332–8338.
- [20] Y. Yang, W.Z. Yang, C.D. Sun, *Sol. Energy Mater. Sol. Cells* 132 (2015) 410–417.
- [21] M. Konagai, K. Takahashi, *J. Appl. Phys.* 46 (1975) 3542–3546.
- [22] C. Feng, Y.J. Zhang, Y.S. Qian, Y. Xu, X.X. Liu, G.C. Jiao, *Opt Commun.* 369 (2016) 50–55.
- [23] Y.J. Zhang, J. Niu, J. Zhao, J.J. Zou, B.K. Chang, F. Shi, H.C. Cheng, *J. Appl. Phys.* 108 (2010), 093108.
- [24] Y.J. Zhang, B.K. Chang, J. Niu, J. Zhao, J.J. Zou, F. Shi, H.C. Cheng, *Appl. Phys. Lett.* 99 (2011) 101104.
- [25] M.C. Jin, B.K. Chang, H.C. Cheng, J. Zhao, M.J. Yang, X.L. Chen, G.H. Hao, *Optik* 125 (2014) 2395–2399.
- [26] D.S. Howarth, D.L. Feucht, *Appl. Phys. Lett.* 23 (1973) 365–367.
- [27] W.E. Spicer, *Phys. Rev.* 112 (1958) 114–122.
- [28] Y. Diao, L. Liu, S.H. Xia, *Sol. Energy* 194 (2019) 510–518.
- [29] C. Feng, Y.J. Zhang, Y.S. Qian, B.K. Chang, F. Shi, G.C. Jiao, J.J. Zou, *Opt Express* 23 (2015) 19478–19488.
- [30] C. Feng, Y.J. Zhang, Y.S. Qian, Z.H. Wang, J. Liu, B.K. Chang, F. Shi, G.C. Jiao, *Opt Commun.* 413 (2018) 1–7.
- [31] M. Levinshtein, M.S. Shur, S. Rumyantsev, *Handbook Series on Semiconductor Parameters*, World Scientific, 1996.
- [32] H.A. Zarem, J.A. Lebens, K.B. Nordstrom, P.C. Sercel, S. Sanders, L.E. Eng, A. Yariv, K.J. Vahala, *Appl. Phys. Lett.* 55 (1989) 2622–2624.
- [33] S. Adachi, *J. Appl. Phys.* 58 (1985) R1–R29.
- [34] D.E. Aspnes, S.M. Kelso, R.A. Logan, R. Bhat, *J. Appl. Phys.* 60 (1986) 754–767.
- [35] <http://www.ioffe.ru/SVA/NSM/nk/index.html>.
- [36] D.G. Fisher, *IEEE Trans. Electron. Dev.* 21 (1974) 541–542.
- [37] D.G. Fisher, R.E. Enstrom, B.F. Williams, *Appl. Phys. Lett.* 18 (1971) 371–373.
- [38] J. Zhao, B.K. Chang, Y.J. Xiong, J.J. Zhang, Y.J. Zhang, *Opt Commun.* 285 (2012) 589–593.